Elastic Visco-Plastic Model for Binary Sand-Clay Mixtures with Applications to One-Dimensional Finite Strain Consolidation Analysis

X. S. Shi[1]; Jianhua Yin[2]; and Jidong Zhao[3]

Abstract: The pore water dissipation of sand–clay mixtures is significantly affected by the sand fraction due to nonuniform stress distribution. On the basis of the elastic visco-plastic modeling concepts of Yin and Graham, a new elastic visco-plastic (EVP) model based on Lagrangian formulation was proposed to consider the effects of sand fraction in a sand–clay mixture on the time-dependent stress–strain behavior at finite strain. In hydraulic dredging and marine deposit improvement projects, the initial water content of mixtures is relatively high, leading to a high compressibility. Therefore, the soil skeleton of the mixtures was fixed to Lagrangian coordinates to facilitate the definition of soil boundary. The governing equation was formulated by combining an equivalent time concept with the mixture theory. A finite difference method was adopted for the benchmark analysis of boundary–initial value problems. The proposed model contained eight parameters. Seven of them pertained to the clay matrix that can be calibrated from the reference time line, instant time line, and consolidation curves of the pure clay in the mixture. The structure parameter represented the intergranular structure and can be calibrated based on the compressibility of a sand–clay mixture. Two multistage oedometer tests (including unloading stages) can be performed to calibrate the model parameters, one on the pure clay and the other on the sand–clay mixture with a predefined sand fraction. A benchmark analysis of the proposed model revealed a significant difference in excess pore pressure dissipation between Eulerian and Lagrangian coordinates. The calibrated model based on Lagrangian coordinates was found to reproduce the effect of sand fraction on the overall responses of sand–clay mixture well when compared with the experimental data of sand–bentonite mixtures and sand–marine clay mixtures from the literature. **DOI: 10.1061/(ASCE)EM.1943-7889.0001623.**

Author keywords: Sand fraction effect; Sand–clay mixtures; Equivalent time; Finite difference method; Mixture theory.

Introduction

Consolidation of clayey soils with continuous gradations has been extensively investigated in progressive deformation and seepage analysis (Yin and Graham 1996; Imai et al. 2003; Xie and Leo 2004; Singh et al. 2014; Zeng et al. 2016). However, natural sedimentary soils are usually gap-graded in terms of particle size distribution due to the presence of certain extents of coarse particles (Satyanaga et al. 2013; Chang et al. 2014; Zhou et al. 2016; Ng et al. 2016; Cui et al. 2017). Human activities may also lead to gap-graded soils, for example, in hydraulic dredging engineering (Deng et al. 2017), land reclamation projects (Yin 1999b; Silva 2016; Shi and Yin 2018c), debris flow-structure interaction mechanisms (Cui et al. 2018), and municipal solid waste (MSW) disposal (Marques et al. 2003; Feng et al. 2014; Hubert et al. 2016). Typically, the soils caused by these activities are a mixture of soft matrix with stiff inclusions (e.g., river sand distributed in clay slurry in hydraulic dredging activities; biodegradation-induced matrix mixed with solid materials in MSW). The hydromechanical behavior of the mixture depends crucially on two levels of soil structure: the intergranular structure of the inclusions and the overall structure of the mixture (Graham et al. 1989; Kumar 1996; Monkul and Ozden 2005, 2007; Cui et al. 2016).

There are two typical hypotheses (termed Hypothesis A and Hypothesis B) that have been proposed in interpreting and modeling the consolidation of clayey soils exhibiting creep (Yin and Feng 2017). In Hypothesis A, a consolidation curve is divided by two separate processes: the primary consolidation coupled with excess pore water pressure dissipation and the secondary consolidation due to viscous deformation after the end of primary consolidation (Mesri and Castro 1987; Mesri 2003). The deformation in primary consolidation can be computed using the classical consolidation theory, for example, Terzaghi's theory for small strain (Cui et al. 2017a, b) and Gibson's theory (Gibson et al. 1967) for finite strain consolidation; the viscous deformation can be calculated separately from a secondary compression index (Mesri and Godlewski 1977; Mesri and Castro 1987). In Hypothesis B, it is assumed that the viscous deformation of the soil skeleton can be induced during and after the primary consolidation process in a coupling process.

The rationality of the Hypothesis B approach can be interpreted within the concept of the dual-porosity structure of clayey soils. De Jong and Verruijt (1965) classified the soil structure into primary and secondary corresponding to primary consolidation and creep deformation, respectively. The secondary structure consists of a cluster of clay particles and micropores between them. The primary structure is composed of clay aggregates (with secondary structure),

[1]Research Assistant Professor, Dept. of Civil and Environmental Engineering, Hong Kong Univ. of Science and Technology, Kowloon, Hong Kong (corresponding author). Email: xiusongshi@ust.hk

[2]Professor, Dept. of Civil and Environmental Engineering, Hong Kong Polytechnic Univ., Hung Hom, Kowloon, Hong Kong. Email: cejhyin@polyu.edu.hk

[3]Associate Professor, Dept. of Civil and Environmental Engineering, Hong Kong Univ. of Science and Technology, Kowloon, Hong Kong. Email: jzhao@ust.hk

Note. This manuscript was submitted on March 22, 2018; approved on December 5, 2018; published online on June 5, 2019. Discussion period open until November 5, 2019; separate discussions must be submitted for individual papers. This paper is part of the ***Journal of Engineering Mechanics***, © ASCE, ISSN 0733-9399.

coarse particles, and macropores. In analogy to aggregated soils and fissured porous media (Valliappan and Khalili-Naghadeh 1990; Borja and Koliji 2009; Choo and Borja 2015; Borja and Choo 2016; Zhao et al. 2017), the hydraulic conductivity associated with the primary structure is considered higher than that arising from the secondary structure. For a given surcharge loading, different hydraulic conductivities lead to a gap of excess pore water pressures and subsequent fluid exchange between the micropores and macropores. This indicates that the primary consolidation and creep occur simultaneously.

In Hypothesis A, the model parameters related to the primary consolidation are calibrated based on the total deformation, which incorporates the creep deformation. Therefore, it is a phenomenological method, which cannot interpret the real deformation mechanism of soils during the progressive deformation. The model based on Hypothesis A can capture most laboratory oedometer data because the soil sample is very thin, only 20 mm, but may not when the soil layer in the field is thick. Time corresponding to the end of primary consolidation is relatively long in the field analysis (usually several years), and the creep deformation during the primary consolidation cannot be neglected. Therefore, the Hypothesis A–based methods significantly underestimate the settlement of thick soil layers in field analysis (Yin and Feng 2017), and Hypothesis B has become increasingly popular (Yin and Graham 1996; Hawlader et al. 2003; Yin and Feng 2017; Huang et al. 2014). In this study, the Hypothesis B approach is adopted for the consolidation analysis of sand–clay mixtures.

In hydraulic dredging and marine deposit improvement projects, the initial water content of the soft soils is relatively high, and a large deformation can be expected (Yin 1999b; Anderson and Lu 2001; Hong et al. 2010; Bian et al. 2019, 2017; Puppala et al. 2017). Therefore, classical small strain theory may be questionable. To this end, both small strain and finite strain concept are incorporated in an elastic visco-plastic model to be proposed subsequently, with further assessment and validation of the model performance.

State Variables and Equivalent Time Lines

State Variables of Sand–Clay Mixtures

A binary sand–clay mixture consisting of soft clay matrix and coarse grain inclusions was considered. The stiffness of the grain inclusions was considered extremely high, such that the overall volume decrease can be regarded solely due to the deformation of the clay matrix during the consolidation process. Consequently, the sand volume fraction ϕ_s (defined as the ratio of the volume of sand inclusions to the overall volume of the mixture) decreased with increasing surcharge loading and can be defined as a function of the overall void ratio of mixtures e

$$\phi_s = \frac{\rho_c - \rho + \rho\upsilon_s}{(1+e)\rho_c} \tag{1}$$

where υ_s is the sand mass fraction, defined as ratio of dry mass of sand inclusions to the overall dry weight of mixtures; ρ is the particle density of mixtures, which can be calculated from the particle densities of the clay matrix ρ_c and the sand inclusions ρ_s

$$\rho = \frac{\rho_c\rho_s}{\upsilon_s\rho_c + (1-\upsilon_s)\rho_s} \tag{2}$$

The local void ratio of the clay matrix e_c can be expressed as

$$e_c = \frac{e\rho_c}{(1-\upsilon_s)\rho} \tag{3}$$

For a given stress level, if the current strains (local strain of the clay matrix ε_c and overall strain of the mixture ε) are known, the corresponding void ratios can be computed from the strains and initial void ratios. Logarithmic strains are defined in this study to consider finite deformation of the mixtures. The incremental strains can be defined as

$$\mathrm{d}\varepsilon = -\mathrm{d}\ln(V_t) = -(1-\phi_s)\mathrm{d}\ln(V_c) = (1-\phi_s)\mathrm{d}\varepsilon_c \tag{4}$$

where V_c and V_t are current volumes of clay matrix and sand–clay mixtures, respectively. The relative difference in stiffness between the clay matrix and coarse inclusions can induce a nonuniform stress in the mixtures (Tandon and Weng 1988; Tu et al. 2005). Volume-average stress variables were considered in the study, according to the following stress relationship in terms of the overall value and constituent:

$$\sigma' = (1-\phi_s)\sigma'_c + \phi_s\sigma'_s \tag{5}$$

where σ' is the overall effective stress of mixtures; and σ'_c and σ'_s is the effective stresses of the clay matrix and sand inclusions, respectively. The definition of stress variables is based on a representative volume element (RVE). The RVE contains statistically representative information of the macrostructure (Zhuang et al. 2014, 2015; Quayum et al. 2015). Within this concept, an increase of its volume size should not lead to apparent changes of state variables or governing equations (Hashin 1983; González et al. 2004; Shi and Herle 2017). This approach was widely adopted in modeling the behavior of polymer-reinforced composites (He et al. 2016) and multiphase geomaterials (Zhuang et al. 2017; Shi et al. 2018a).

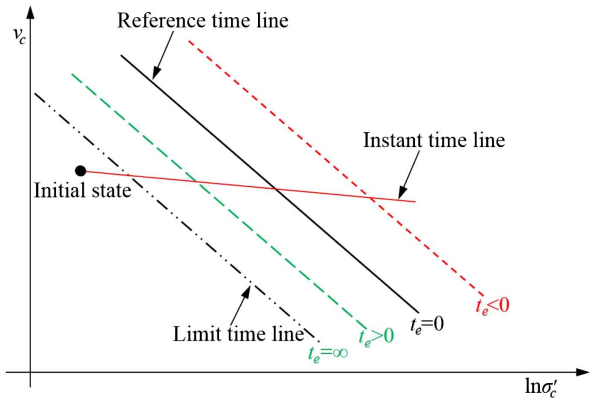

Fig. 1. Equivalent time lines for clay matrix in sand–clay mixtures.

Equivalent Time Lines of Clay Matrix

The coarse particles are assumed to be incompressible; thus, the hydromechanical behavior of the soft clay matrix can be introduced as a reference for evaluating the behavior of the mixtures. The equivalent time concept of the clay matrix will be presented in the sequel of this section. The concept of time lines was proposed by Bjerrum (1967) for interpreting the stress–strain-time relationship of clayey soils. Yin and Graham (1994) provided further mathematical description for the time line concept. They assumed that the deformation was composed of elastic and visco-plastic parts. Following their definitions, the time lines of the clay matrix are shown in Fig. 1 in terms of the σ'_c-v_c relationship ($v_c = e_c + 1$), including the instant, reference, limit, and equivalent time lines (dotted lines).

The instant time line describes the instant deformation behavior accompanying the dissipation of excess pore water pressures. Semilogarithmic functions between v_c and σ_c' were used in this study. The instant incremental value of v_c is given as

$$\mathrm{d}v_c^e = -\frac{\kappa_c}{\sigma_c'}\mathrm{d}\sigma_c' \tag{6}$$

where κ_c is the slope of the instant time line semilogarithmic v_c-σ_c' plot. The equivalent time t_e is defined as the time duration for creep from the reference time line to the current state (σ_c', v_c) at a given stress level (Yin and Graham 1994). The equivalent time lines in Fig. 1 represent unique v_c-σ_c' relationships for constant values of equivalent time. The reference time line is the equivalent time line at $t_e = 0$. The equivalent time is negative above the reference time line and becomes positive below the reference time line. The reference time line can be expressed as

$$v_c^{\mathrm{ref}} = N_c - \lambda_c \ln\left(\frac{\sigma_c'}{\sigma_r}\right) \tag{7}$$

where N_c and λ_c are the model parameters for the reference line of clay matrix; and $\sigma_r = 1$ kPa is a reference stress. The values of N_c and λ_c are affected by the initial water content of clayey soils (e.g., Hong et al. 2010; Shi and Herle 2015; Horpibulsuk et al. 2016). Hence, the initial water content of the clay matrix in a mixture should be consistent with the pure clay for analysis. A linear creep function was adopted in this work as follows:

$$v_c^{tp} = -\psi_c \ln\left(\frac{t_0 + t_e}{t_0}\right) \tag{8}$$

where t_0 is the curve-fitting parameter responsible for the reference time line. The linear creep function gives a satisfactory performance for a time duration of practical interest. However, the creep diminishes with the creep time, and finally reaches the limit time line in Fig. 1. To describe the long-term creep behavior, one can use the nonlinear creep function proposed by Yin (1999a). Within the equivalent time concept, the time-dependent deformation behavior follows a relationship between v_c, σ_c', and t_e

$$v_c = v_c^{\mathrm{ref}} + v_c^{tp} = N_c - \lambda_c \ln\left(\frac{\sigma_c'}{\sigma_r}\right) - \psi_c \ln\left(\frac{t_0 + t_e}{t_0}\right) \tag{9}$$

Eq. (9) indicates that the current specific volume of the clay matrix can be approximated by the specific volume at the reference time line under the same effective stress with further creep deformation. The equivalent time can be derived as

$$t_e = t_0 \exp\left(\frac{N_c - v_c}{\psi_c}\right)\left(\frac{\sigma_c'}{\sigma_r}\right)^{-\frac{\lambda_c}{\psi_c}} - t_0 \tag{10}$$

Elastic Visco-Plastic Model

Governing Equation within Eulerian Coordinates

The increment of specific volume of clay matrix consists of the elastic part $\mathrm{d}v_c^e$ and visco-plastic part $\mathrm{d}v_c^{tp}$. Considering Eqs. (6) and (8), one gets

$$\mathrm{d}v_c = \mathrm{d}v_c^e + \mathrm{d}v_c^{tp} = -\frac{\kappa_c}{\sigma_c'}\mathrm{d}\sigma_c' - \frac{\psi_c}{t_0 + t_e}\mathrm{d}t \tag{11}$$

The elastic part is an instant incremental one associated with the stress level and its increment. Eq. (9) is another interpretation of the current specific volume of the clay matrix. The specific volume on the reference time line can be further decomposed into two parts: the specific volume on the instant time line and a visco-plastic part (a constant value, being expressed as a difference between the instant time line and the reference time line). In this case, the incremental form of Eq. (9) is consistent with Eq. (11).

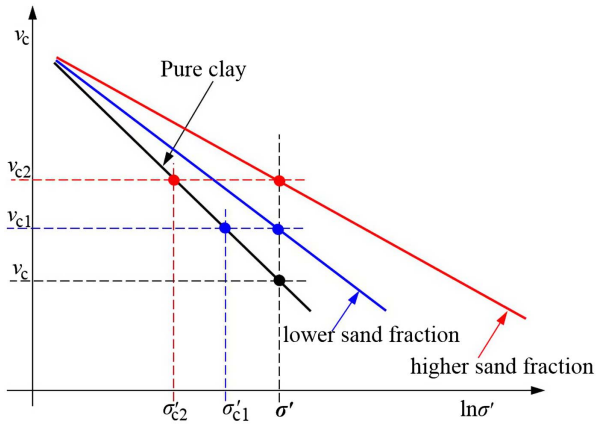

Fig. 2. Nonuniform state variables in binary sand–clay mixtures.

Typical reference time lines of the clay mixtures in sand–clay mixtures are shown in Fig. 2. The line with a higher sand fraction is located above that with a lower sand fraction. This phenomenon is induced by nonuniform stress distribution in the mixtures. An incremental stress ratio μ_σ^c is defined as

$$\mu_\sigma^c = \frac{\mathrm{d}\sigma_c'}{\mathrm{d}\sigma'} \tag{12}$$

Substitution of Eqs. (10) and (12) into Eq. (11) and applying the effective stress principal to Eq. (11) gives

$$\frac{\partial v_c}{\partial t} = -\mu_\sigma^c \frac{\kappa_c}{\sigma_c'}\frac{\partial(\sigma - p)}{\partial t} - \frac{\psi_c}{t_0}\exp\left(\frac{v_c - N_c}{\psi_c}\right)\left(\frac{\sigma_c'}{\sigma_r}\right)^{\frac{\lambda_c}{\psi_c}} \tag{13}$$

where σ and ρ are the total stress and excess pore water pressure in sand-clay mixtures. Eq. (13) offers a unique relationship between $\partial v_c/\partial t$, σ_c', $\partial\sigma_c/\partial t$, and v_c. The incremental relationship between the specific volume and the strain of the clay matrix can be written as

$$\frac{\partial v_c}{\partial t} = v_c \frac{\partial \ln(v_c)}{\partial t} = -v_c \frac{\partial \varepsilon_c}{\partial t} \tag{14}$$

The volume change due to deformation equals the volume of water out of a soil element. The condition of continuity adopted in classical consolidation theory within Eulerian coordinates is

$$\frac{\partial \varepsilon_c}{\partial t} = -\frac{k_c}{\gamma_w}\frac{\partial^2 p_c}{\partial z^2} \tag{15}$$

where γ_w is the unit weight of water; z is the one-dimensional (1D) space variable in Eulerian coordinates; k_c is the hydraulic conductivity of the clay matrix; and p_c is the excess pore water pressure in the clay matrix. Considering that the coarse particles are impermeable with no water holding capacity (Mitchell 1993), the overall excess pore water pressure p is the local value p_c. Combining Eqs. (13)–15 yields (considering that $\partial\sigma/\partial t = 0$)

$$\frac{k_c}{\gamma_w}\frac{\partial^2 p}{\partial z^2} = \mu_\sigma^c \frac{\kappa_c}{v_c\sigma_c'}\frac{\partial p}{\partial t} - \frac{\psi_c}{v_c t_0}\exp\left(\frac{v_c - N_c}{\psi_c}\right)\left(\frac{\sigma_c'}{\sigma_r}\right)^{\frac{\lambda_c}{\psi_c}} \tag{16}$$

The incremental stress ratio is a state-dependent parameter. From the equivalent time lines, one obtains the tangent stiffness of the clay matrix

J. Eng. Mech., 2019, 145(8): 04019059

$$\frac{\mathrm{d}\sigma_c'}{\mathrm{d}\varepsilon_c} = \frac{v_c\sigma_c'}{\lambda_c} \tag{17}$$

After Shi and Yin (2017), the tangent stiffness of sand–clay mixtures can be approximated by that of the clay mixtures and an additional structure variable

$$\frac{\mathrm{d}\sigma'}{\sigma_r \mathrm{d}\varepsilon} = \left(\frac{\mathrm{d}\sigma_c'}{\sigma_r \mathrm{d}\varepsilon_c}\right)^{\eta(1-\phi_s)} \tag{18}$$

where η is a structure variable associated with the intergranular structure, which depends on the sand volume fraction

$$\eta = \left(\frac{1}{1-\phi_s(1+\tilde{e}_s)}\right)^{\vartheta} \tag{19}$$

where ϑ is a model parameter; and $\tilde{e}_s$ is the minimum void ratio of the sand material.

Combining Eqs. (4), (12), (17), and (18), the incremental stress ratio is deduced as

$$\mu_\sigma^c = \left(\frac{v_c\sigma_c'}{\lambda_c\sigma_r}\right)^{1-\eta(1-\phi_s)} \tag{20}$$

Substitution of Eq. (20) into Eq. (16) gives

$$\frac{k_c}{m_v\gamma_w}\frac{\partial^2 p}{\partial z^2} = \left(\frac{v_c\sigma_c'}{\lambda_c\sigma_r}\right)^{1-\eta(1-\phi_s)}\frac{\partial p}{\partial t} - \frac{\sigma_c\psi_c}{\kappa_c t_0}\exp\left(\frac{v_c-N_c}{\psi_c}\right)\left(\frac{\sigma_c'}{\sigma_r}\right)^{\frac{\lambda_c}{\psi_c}} \tag{21}$$

where $m_v = \kappa_c/(v_c\sigma_c')$ is the compression coefficient following the instant time line.

Governing Equation in Lagrangian Coordinates

As stated previously, the governing equation formulated within Eulerian coordinates is questionable in the case of large strain problems with moving boundaries. In this section, the governing equation will be reformulated within the Lagrangian coordinates.

Considering a soil element in one-dimensional consolidation, z and ζ are 1D space variables in Eulerian and Lagrangian coordinates, respectively. The variable ζ is independent of the consolidation time; thus, the boundary condition can be easily defined. Continuity of the solid phase in sand–clay mixtures (consisting of clay and sand particles) in the soil element gives

$$\frac{\partial z}{\partial t}[1-(1-\phi_s)n_c] = \frac{\partial \zeta}{\partial t}[1-(1-\phi_{s0})n_{c0}] \tag{22}$$

where n_c is the porosity of the clay matrix; and n_{c0} is the corresponding initial value. Considering that $(1-\phi_s)n_c = e/(1+e)$, Eq. (22) can be rearranged as

$$\frac{\partial z}{\partial \zeta} = \frac{1+e}{1+e_0} \tag{23}$$

The condition of continuity for water in the clay matrix (the volume change due to deformation equals the volume of water out of a soil element) gives

$$\frac{\partial}{\partial \zeta}[(1-\phi_s)n_c v_{cr}] = -\frac{\partial}{\partial t}\left((1-\phi_s)n_c\frac{\partial z}{\partial \zeta}\right) \tag{24}$$

where $v_{cr} = v_f - v_{cs}$ is the relative velocity of fluid in the clay matrix, with v_f denoting the absolute velocity of the fluid and v_{cs} being the absolute velocity of soil particles in the matrix.

The relative fluid velocity in Eq. (24) is associated with the pore water pressure in the clay matrix using Darcy's law

$$(1-\phi_s)n_c v_{cr} = -\frac{k_c}{\gamma_w}\frac{\partial p_c}{\partial z} = -\frac{k_c}{\gamma_w}\frac{\partial p}{\partial z} \tag{25}$$

where n_c = porosity of the clay matrix. Substitution of Eqs. (23) and (25) into Eq. (24) yields

$$\frac{(1+e_0)^2}{\gamma_w}\frac{\partial}{\partial \zeta}\left(\frac{k_c}{1+e}\frac{\partial p}{\partial \zeta}\right) = \frac{\partial e}{\partial t} \tag{26}$$

The increment of the overall void ratio is expressed as

$$\frac{\partial e}{\partial t} = -v\frac{\partial \varepsilon}{\partial t} = -v(1-\phi_s)\frac{\partial \varepsilon_c}{\partial t} \tag{27}$$

Combining Eqs. (13), (14), (26), and (27), one obtains the governing equation and the overall strain increment for the consolidation analysis (see Appendix)

$$\frac{(1+e_0)^2 k_c}{(1+e)^2\gamma_w m_v}\frac{\partial^2(\ln\sigma')}{\partial\zeta^2} = (1-\phi_s)\mu_\sigma^c\frac{\partial(\ln\sigma')}{\partial t} + (1-\phi_s)\frac{\sigma_c'\psi_c}{\sigma'\kappa_c t_0}\exp\left(\frac{v_c-N_c}{\psi_c}\right)\left(\frac{\sigma_c'}{\sigma_r}\right)^{\frac{\lambda_c}{\psi_c}} \tag{28}$$

$$\frac{\partial \varepsilon}{\partial t} = (1-\phi_s)\mu_\sigma^c m_v\frac{\partial \sigma'}{\partial t} + (1-\phi_s)\frac{\psi_c}{v_c t_0}\exp\left(\frac{v_c-N_c}{\psi_c}\right)\left(\frac{\sigma_c'}{\sigma_r}\right)^{\frac{\lambda_c}{\psi_c}} \tag{29}$$

The permeability of the clay matrix is a state variable, which can be approximated by a power law of the local void ratio for the clay matrix according to Mesri and Olson (1971) and widely used by others (Pane and Schiffman 1997; Dolinar 2009; Zeng et al. 2012)

$$\ln(k_c/k_r) = A_c + \xi_c \ln e_c \tag{30}$$

where $k_r = 1$ m/s is a unit reference value; A_c and ξ_c are model parameters; ξ_c is the slope of the permeability curve in double logarithmic relationship; and A_c corresponds to a unit void ratio.

Numerical Solution Procedure

Initial and Boundary Conditions

Only initial and boundary conditions within Lagrangian coordinates are discussed. To solve the governing equation in Eq. (28), two kinds of boundary conditions are considered: the stress and seepage boundaries. Accordingly, two boundaries, $\Gamma 1$ for effective stress and $\Gamma 2$ for stress gradient, are defined. The boundary conditions in Lagrangian coordinates are given as

$$\sigma'(\zeta,t) = \bar{\sigma}(\zeta,t); \quad \zeta \in \Gamma 1, t \in [0,\infty) \tag{31a}$$

$$\frac{\partial \sigma'(\zeta,t)}{\partial \zeta} = \bar{q}(\zeta,t); \quad \zeta \in \Gamma 2, t \in [0,\infty) \tag{31b}$$

where $\bar{\sigma}'(\zeta,t)$ and $\bar{q}(\zeta,t)$ are the loading stress and prescribed value fluid flow on the boundary, respectively. A uniform initial effective stress of the investigated domain is given as

$$\sigma'(\zeta,0) = \bar{\sigma}_0'(\zeta) \tag{32}$$

J. Eng. Mech., 2019, 145(8): 04019059

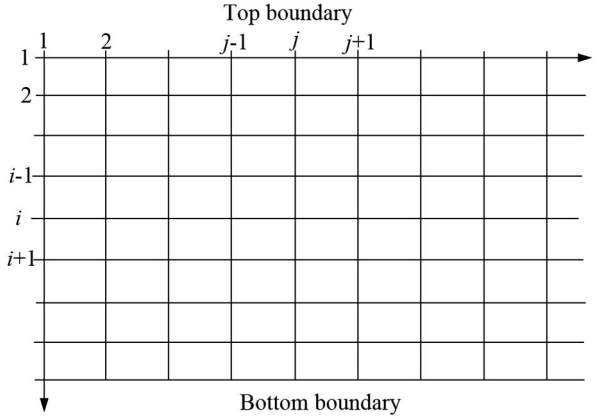

Fig. 3. Configuration for finite difference analysis.

Finite Difference Approach

Combining Eqs. (28) and (29) and (31*a*)–(32), the consolidation analysis of sand–clay mixtures can be performed using the finite difference method. The configuration of the finite difference model is shown in Fig. 3. In Lagrangian coordinates, the domain is bounded by the lines $\zeta = 0$ and $\zeta = h$ (h is the thickness of the soil layer) for 1D consolidation analysis. The domain is further discretized into equal rectangles of size $\delta\zeta$ along the ζ axis, with i and j referring to the ζ (depth) and t (time) coordinates, respectively. For point (i, j) in the grid, the governing Eq. (28) can be approximated by the following difference equations:

$$\left(\frac{(1+e_0)^2}{2(1+e)^2(1-\phi_s)}c_v\right)_i^j \frac{\tilde{\sigma}_{i+1}^{j+1}+\tilde{\sigma}_{i-1}^{j+1}-2\tilde{\sigma}_i^{j+1}+\tilde{\sigma}_{i+1}^{j}+\tilde{\sigma}_{i-1}^{j}-2\tilde{\sigma}_i^{j}}{(\delta\zeta)^2} = \frac{(\mu_\sigma^c)_i^j}{\delta t}(\tilde{\sigma}_i^{j+1}-\tilde{\sigma}_i^j)+\left(\frac{\sigma_c'}{\sigma'\kappa_c}w\right)_i^j \tag{33a}$$

$$\tilde{\sigma} = \ln(\sigma'); \qquad c_v = \frac{k_c}{\gamma_w m_v}; \qquad w = \frac{\psi_c}{t_0}\exp\left(\frac{v_c - N_c}{\psi_c}\right)\left(\frac{\sigma_c'}{\sigma_r}\right)^{\frac{\lambda_c}{\psi_c}} \tag{33b}$$

Eq. (33) can be rearranged as

$$f_i^j\tilde{\sigma}_{i-1}^{j+1} - [2f_i^j + (\mu_\sigma^c)_i^j]\tilde{\sigma}_i^{j+1} + f_i^j\tilde{\sigma}_{i+1}^{j+1} = g_i^j \tag{34a}$$

$$f_i^j = \left(\frac{(1+e_0)^2}{2(1+e)^2(\delta\zeta)^2(1-\phi_s)}c_v\right)_i^j \delta t \tag{34b}$$

$$g_i^j = -f_i^j\tilde{\sigma}_{i-1}^j - \left[(\mu_\sigma^c)_i^j - 2f_i^j\right]\tilde{\sigma}_i^j - f_i^j\tilde{\sigma}_{i+1}^j + \left(\frac{\sigma_c}{\sigma'\kappa_c}w\right)_i^j \delta t \tag{34c}$$

From Eq. (29), the overall strain at the current incremental step can be computed as

$$\varepsilon_i^{j+1} = \varepsilon_i^j + [(1-\phi_s)m_v]_i^j(\mu_\sigma^c)_i^j(\sigma_i^{j+1}-\sigma_i^j) + \left((1-\phi_s)\frac{w}{v_c}\right)_i^j \delta t \tag{35}$$

Eq. (34*a*) can be written as the following form:

$$\begin{pmatrix} \alpha_1 & \beta_1 & 0 & 0 & 0 & 0 \\ f_2^j & -2f_2^j-(\mu_\sigma^c)_2^j & f_2^j & 0 & 0 & 0 \\ 0 & f_3^j & -2f_3^j-(\mu_\sigma^c)_3^j & f_3^j & 0 & 0 \\ \cdots & \cdots & \cdots & \cdots & \cdots & \cdots \\ 0 & 0 & 0 & f_{n-1}^j & -2f_{n-1}^j-(\mu_\sigma^c)_{n-1}^j & 0 \\ 0 & 0 & 0 & 0 & \alpha_2 & \beta_2 \end{pmatrix} \begin{pmatrix} \tilde{\sigma}_1^{j+1} \\ \tilde{\sigma}_2^{j+1} \\ \tilde{\sigma}_3^{j+1} \\ \cdots \\ \tilde{\sigma}_{n-1}^{j+1} \\ \tilde{\sigma}_n^{j+1} \end{pmatrix} = \begin{pmatrix} g_1^j \\ g_2^j \\ g_3^j \\ \cdots \\ g_{n-1}^j \\ g_n^j \end{pmatrix} \tag{36}$$

The boundary conditions can be described by choosing suitable values of α_1, β_1, α_2, and β_2. If the top (bottom) boundary is freely draining, $\alpha_1 = 1$; $\beta_1 = 0$, $g_1^j = \ln(\bar{\sigma})$ ($\alpha_2 = 0$, $\beta_2 = 1 g_n^j = \ln(\bar{\sigma})$). For impermeable top (bottom) boundary, $\alpha_1 = \beta_1, g_1^j = 0$ ($\alpha_2 = \beta_2, g_n^j = 0$). The numerical procedures for the consolidation analysis of the sand–clay mixtures are presented in Fig. 4.

Model Evaluation

Model Parameters

The proposed elastic visco-plastic model has eight principal parameters: two of them are related to the reference time line of the clay matrix, N_c and λ_c; κ_c corresponds to the instant time line of the clay matrix; A_c and ξ_c are intrinsic permeability parameters. Among the creep parameters, t_0 is the indicator for the beginning of the creep time and t_e (end of primary consolidation), and ψ_c denotes the creep coefficient of the clay matrix. The parameter ϑ is a structure parameter incorporating the evolution of the intergranular structure of the sand skeleton. The values of N_c, λ_c, κ_c, t_0, and ψ_c can be calibrated from an oedometer test of the pure clay. The calibration procedure followed that described in Yin and Graham (1994).

The calibration of the permeability parameters (A_c and ξ_c) and the structure parameter ϑ is given as follows: the permeability k_c was computed from the compressibility and consolidation curves of the pure clay matrix based on the following equation (Shi and Yin 2018b):

$$k_c = \frac{\lambda_c c_v \gamma_w}{\sigma_c'} \tag{37}$$

where $c_v = 0.212h^2/t_{90}$ is the coefficient of consolidation of the pure marine clay; h is the height of the specimen; and t_{90} (s) is the time duration at 90% of consolidation. The permeability parameters A_c and ξ_c can be calibrated from the permeability data points

(k_c and e_c in a double logarithmic plot) at different stress levels. As summarized by Shi and Yin (2018b), the ranges of the permeability parameters are −35 to −22 for A_c and 3.5 to 6.7 for ξ_c. The structure parameter ϑ can be calibrated based on two oedometer tests: one on the pure clay and the other on the mixture with a predefined fraction of sand particles. It can be determined from the relationship between the structure variable η and the sand volume fraction ϕ_s. The value of the structure parameter ϑ for different soils varies

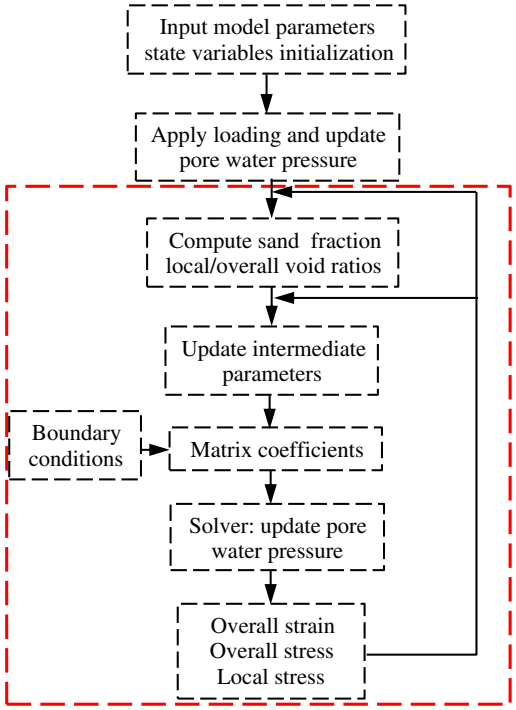

Fig. 4. Flow chart for the consolidation analysis of sand–clay mixtures using finite difference method.

Table 1. Model parameters for benchmark analysis and validation of the proposed model

Parameters	Benchmark analysis	Sand–bentonite	Sand–marine clay
N_c	20	22	3.33
λ_c	2.50	2.75	0.22
κ_c	1.0	0.94	0.07
t_0 (min)	1,440	1,440	100
ψ_c	0.10	Eq. (38)	0.007
A_c	−30.0	−34.0	−22.7
ξ_c	4.00	4.18	4.15
ϑ	0.80	0.80	0.75

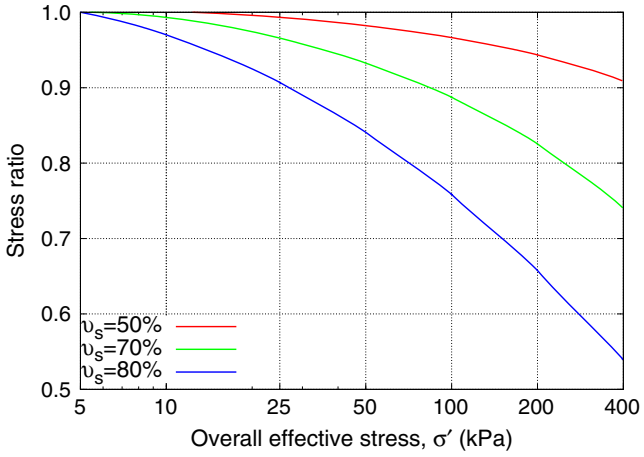

Fig. 6. Evolution of stress ratio in oedometer compression (middle of the sample) within Eulerian coordinates.

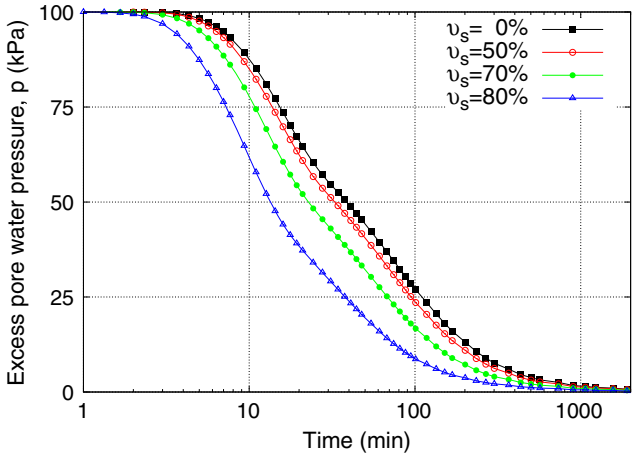

Fig. 7. Evolution of excess pore water pressure (middle of the sample) within Eulerian coordinates (100–200 kPa).

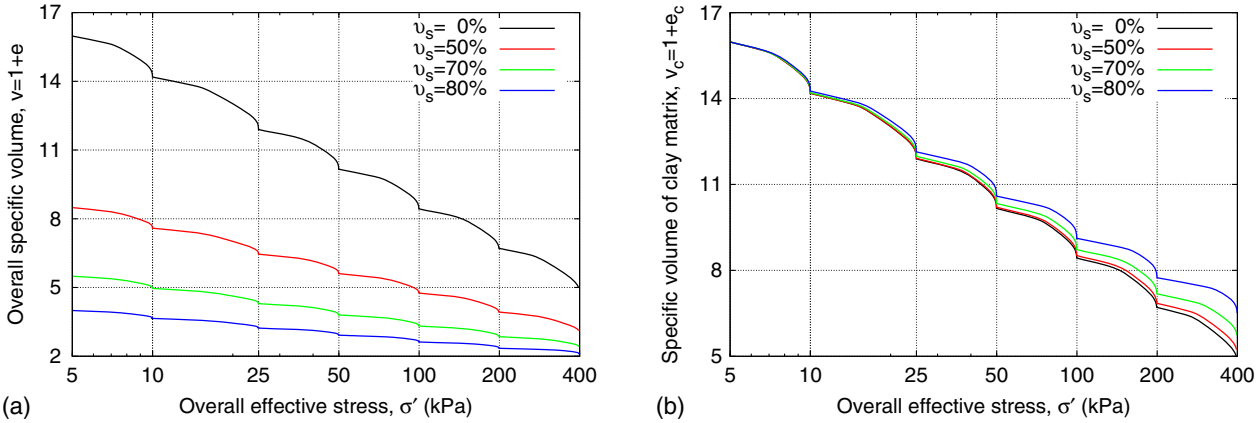

Fig. 5. Consolidation analysis of sand–clay mixtures within Eulerian coordinates: (a) overall specific volume; and (b) local specific volume.

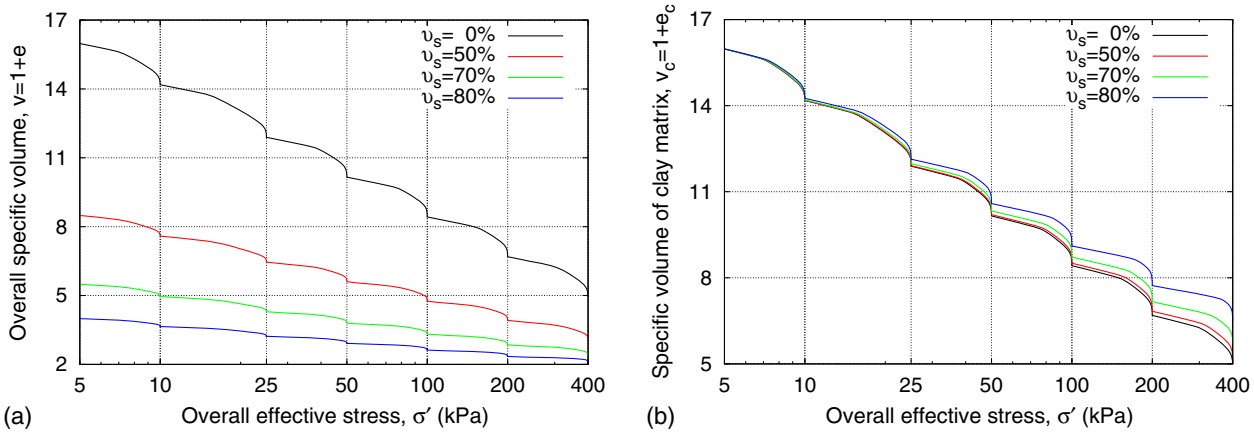

Fig. 8. Consolidation analysis of sand–clay mixtures within Lagrangian coordinates: (a) overall specific volume; and (b) local specific volume.

within a narrow range, from 0.7 (low-plasticity clay) to 0.8 (high-plasticity clay).

Benchmark Analysis of the Model

This section presents benchmark examples for the consolidation analysis of mixtures, including both Eulerian and Lagrangian coordinates and their comparisons. The one in Eulerian coordinates can be regarded as extended from the model proposed by Yin and Graham (1994), and the original model after Yin and Graham (1994) recovers if the sand fraction is reduced to 0. Other elastic visco-plastic (EVP) models based on Hypothesis A, for example, the ones proposed by Hinchberger et al. (2010) and Chang and Zoback (2010), may not be particularly suitable for coupling hydro-mechanical analysis of saturated sand–clay mixtures.

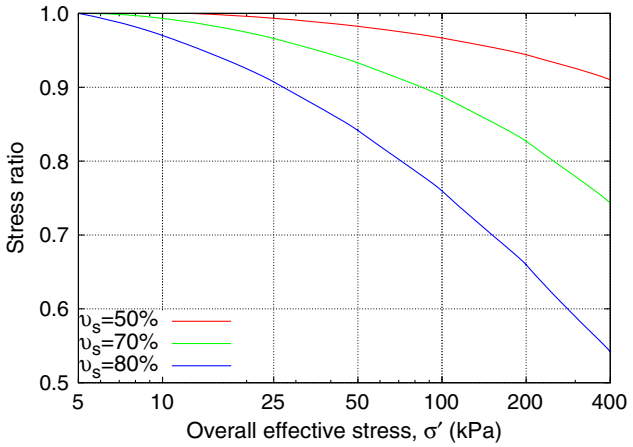

Fig. 9. Evolution of stress ratio in oedometer compression (middle of the sample) within Lagrangian coordinates.

Consider a thin soil layer with a thickness of $h = 2$ cm subjected to a uniform surcharge loading on both the top ($\zeta = 0$) and bottom $\zeta = h$ surfaces. Both surfaces were assumed to be free drain. The minimum void ratio of the sand material was 0.54, and the clay and sand particles were assumed to have the same density of 2,650 kg/m^3. The model parameters are given in Table 1. The soil layer was discretized with 200 nodes, with a uniform initial effective stress of 5 kPa. The initial states of the mixtures were assumed to be on the reference time lines. Six steps of subsequent surcharge loading were applied: 5, 10, 25, 50, 100, and 200 kPa. The state variables (excess pore water pressure, effective stress, and stress ratio) at the middle of the soil layer were recorded during the simulation.

Fig. 5(a) shows the compression curves of the sand clay mixtures in terms of overall specific volume and overall effective stress in Eulerian coordinates. It is seen that the pattern of compression curves was different from the reference time lines. The compression curves were nonlinear due to the coupling of excess pore water dissipation and time-dependent deformation. The local deformation of

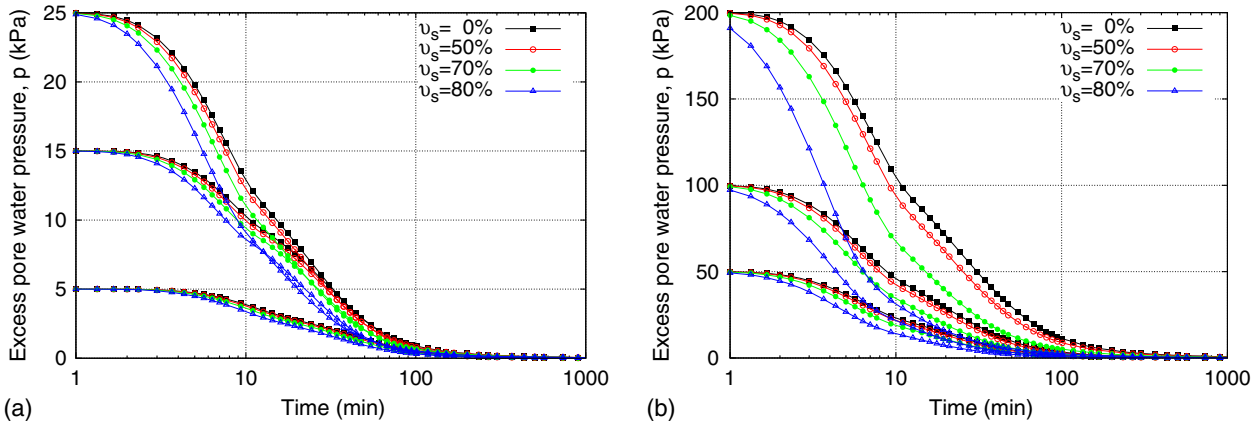

Fig. 10. Evolution of excess pore water pressure at different stress levels (middle of the sample) within Lagrangian coordinates: (a) pore water pressure increments of 5, 15, and 25 kPa; and (b) pore water pressure increments of 50, 100, and 200 kPa.

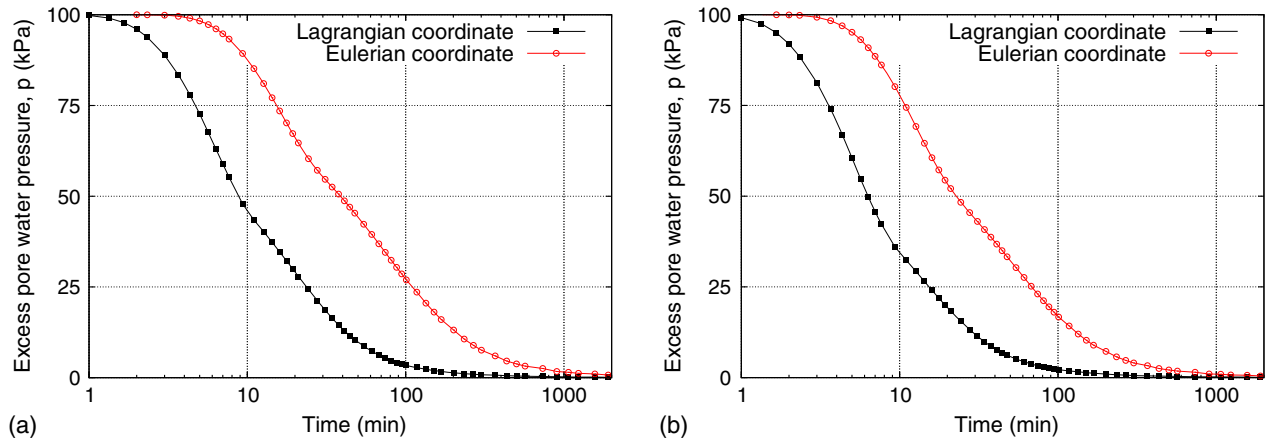

Fig. 11. Evolution of excess pore water pressure within Eulerian and Lagrangian coordinates (100–200 kPa): (a) $v_s = 0\%$; and (b) $v_s = 70\%$.

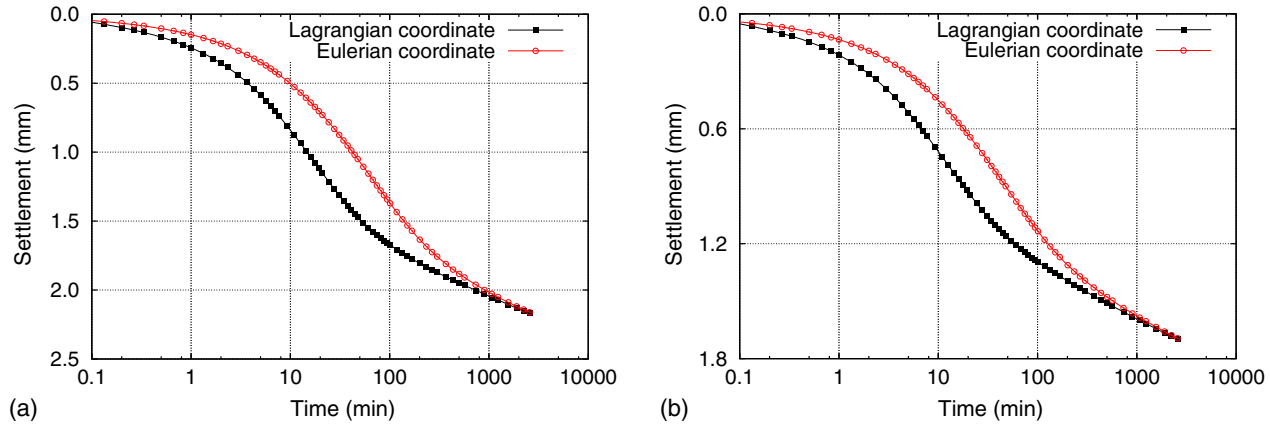

Fig. 12. Settlement of the sand–clay mixtures within Eulerian and Lagrangian coordinates (100–200 kPa): (a) $v_s = 0\%$; and (b) $v_s = 70\%$.

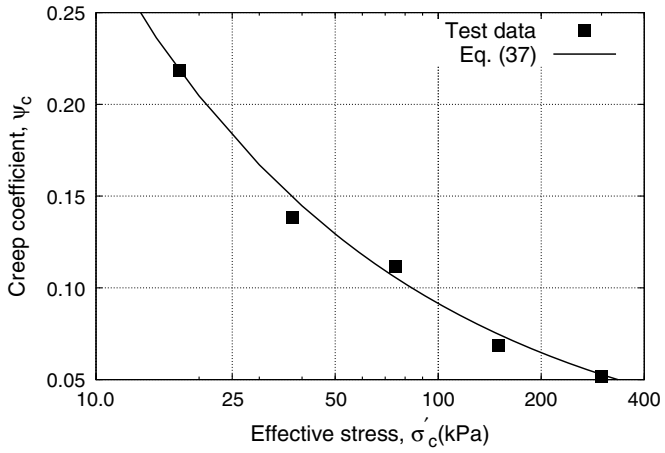

Fig. 13. Change of creep coefficient of bentonite matrix.

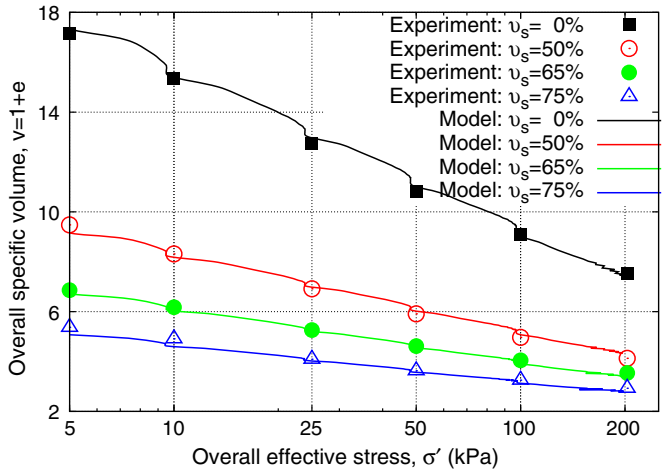

Fig. 14. Comparison between the experimental data and the model simulation in v-σ' compression plane (sand–bentonite mixtures).

the mixtures is depicted in Fig. 5(b). The compression curves of the mixture gradually deviated from the corresponding ones of the pure clay with the increase of both sand mass fraction and stress level. This can be explained by the evolution of the incremental stress ratio in Fig. 6: the volume fraction of sand increased with sand mass fraction and stress level. Correspondingly, the incremental stress ratio decreased [refer to Eqs. (19) and (20)], and the clay matrix showed a smaller compressibility.

The excess pore water pressure dissipation of the mixtures (loading increment of 100 kPa) is shown in Fig. 7 in a semilogarithmic plot. For a low sand mass fraction (50%), the consolidation curve of the mixture is relatively close to the one of pure clay. However, the consolidation process was accelerated with further increase of the sand fraction. This is due to the different evolution of local stress in the clay matrix. As shown in Fig. 6, at the same surcharge, loading the local stress in the clay matrix decreased with the sand fraction. Consequently, a higher local void ratio and higher permeability of the clay matrix can be expected for the mixture with a higher sand mass fraction, and this induces a more rapid pore water pressure dissipation.

The consolidation data (including the compression curves, excess pore water pressure dissipation, and stress ratio) of the mixtures in Lagrangian coordinates are presented in Figs. 8–10. The compression curves and incremental stress ratio evolution are approximately the same as the corresponding ones in Eulerian coordinates. Fig. 10 presents the excess pore water pressure dissipation at all loading steps. The consolidation curves with different sand fractions almost overlapped at loading increments of 5 kPa because the local stresses in the matrix were close, and the incremental stress ratio was higher than 0.9. With increasing stress level, the consolidation process was significantly affected by the sand fraction. The consolidation curves of the pure clay and mixture ($\upsilon_s = 70\%$) are plotted in the same figures (Fig. 11), highlighting

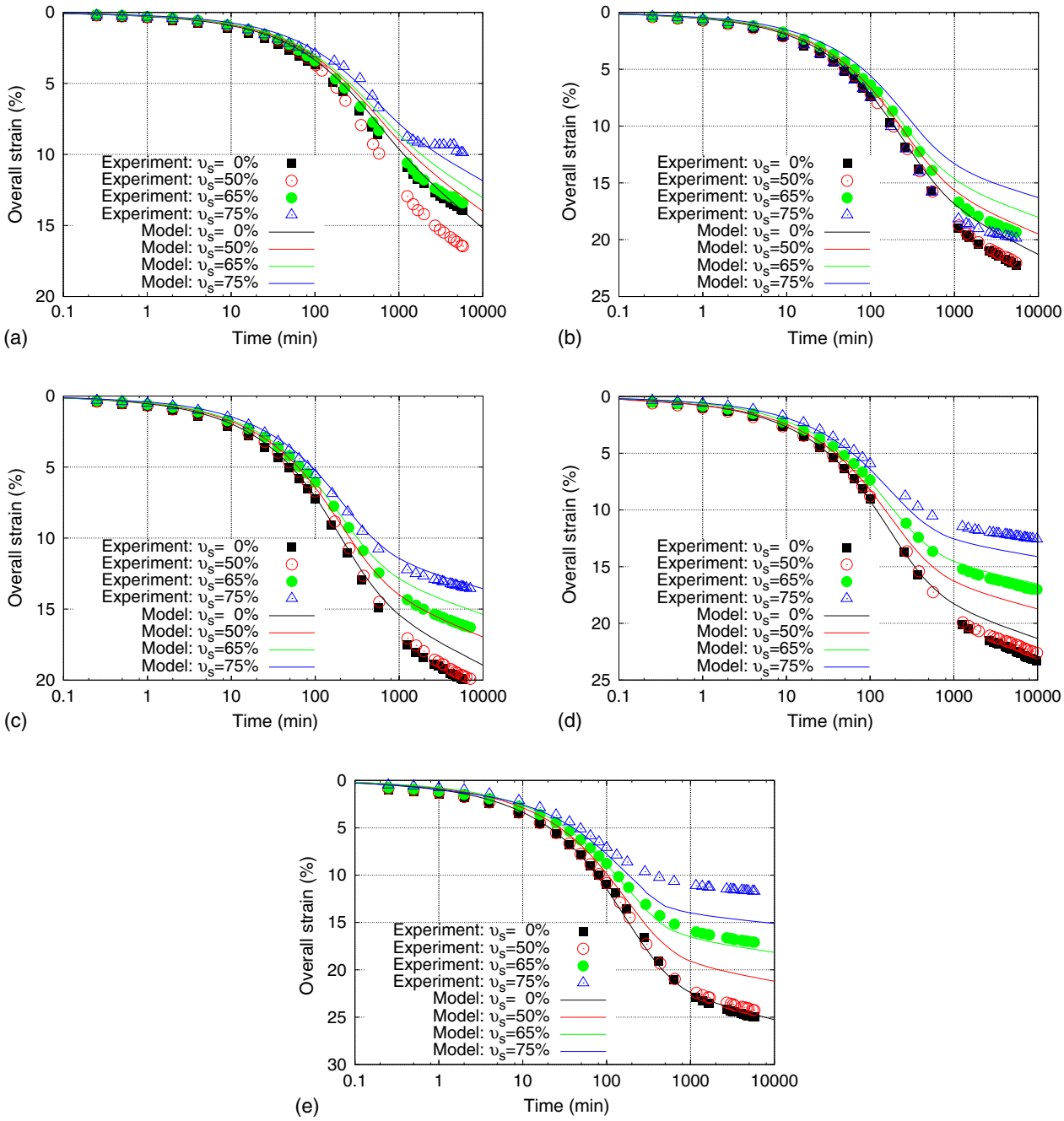

Fig. 15. Comparison between the experimental data and model simulation based on Lagrangian coordinates (sand–bentonite mixtures): (a) 5–10 kPa; (b) 10–25 kPa; (c) 25–50 kPa; (d) 50–100 kPa; and (e) 100–200 kPa.

J. Eng. Mech., 2019, 145(8): 04019059

the difference caused by the use of the two coordinates. The soil skeleton of the mixtures and the boundaries were fixed to the Lagrangian coordinates. Therefore, the time-dependent boundaries can be defined, and a more rapid dissipation of the excess pore water pressure can be expected due to decreasing thickness of the consolidating soil layer. The settlement of the pure clay and mixture ($\upsilon_s = 70\%$) within Eulerian and Lagrangian coordinates is shown in Fig. 12 (loading increment of 100 kPa). The final settlements were almost the same in the two cases. However, due to different rates of dissipation, the settlements were different during the primary consolidation process.

Validation of the Model

Section "Model Evaluation" indicates the consolidation model in Lagrangian coordinates is more reasonable. It was adopted for comparison with the experimental data from literature. Two sand–clay mixtures exhibiting significantly different creep behavior were presented for the validation: (1) the sand–marine clay mixtures (data from Shi and Yin 2018c) with a small creep coefficient, and (2) the sand–bentonite mixtures [data from Shi et al. (2018d)] showing a large creep deformation. The oedometer tests on the two mixtures followed the same procedure: first, water was added to the dry clay matrix to get slurries with desired initial water contents. The matrix slurry and sand particles were then mixed homogeneously for a given sand fraction. Finally, the sample was poured into a cutting ring, and the consolidation stress was increased stepwise. For more details on the test procedure, one can refer to Shi et al. (2018a) and Shi and Yin (2018c).

Sand–Bentonite Mixtures

The mixture consisted of bentonite matrix and silicon sand inclusions. The particle size of silicon sand ranges from 1.0 to 2.0 mm. The minimum void ratio of the sand material was 0.55. The particle densities of the constituents were 2,690 and 2,700 kg/m^3 for the sand and clay particles, respectively. Due to the extremely high liquid limit of the bentonite matrix, the initial water content of the clay matrix was as high as 885%. Mixtures with four different sand fractions (0%, 50%, 65%, and 75%) were tested. The time duration at a given stress level was more than 5,000 min, and the loading period was more than 10,000 min at the consolidation stress of 100 kPa. The creep coefficient of the bentonite matrix showed significant variation within the test stress range. It can be approximated by a function of the effective stress (Fig. 13)

$$\psi_c = 0.92\left(\frac{\sigma_c'}{\sigma_r}\right)^{-0.5} \tag{38}$$

The effective stress σ_c' is the average stress of the initial and final values of a given consolidation stress.

Sand–Marine Clay Mixtures

The data of the sand–marine clay matrix follow those presented by Shi and Yin (2018c). The mixture was composed of Hong Kong marine deposits and a coarse sand material, with four sand mass fractions (0%, 20%, 40%, 60%). The minimum void ratio of the sands was 0.601. The liquid limit of the marine clay was 62.4%, and the initial water content of the clay matrix was 86.9%. The particle densities of the sand and clay matrix were 2,630 and 2,680 kg/m^3, respectively. The parameter t_0 related to the reference time line was 100 min. The creep coefficient of the marine clay matrix varied within a narrow range (0.005–0.009); thus, an average value of 0.007 was adopted for the simulation.

Evaluation of the Model

The data at small stress levels (blew 5 kPa) were excluded from analysis. Following the laboratory testing in Shi and Yin (2018c), both the top and bottom surfaces were assumed to be free draining. A uniform initial stress of 5 kPa was assumed. The model parameters for the sand–marine clay matrix and sand bentonite matrix are listed in Table 1. The model parameter $t_0 = 1440$ min. The initial void ratios of the bentonite and marine clay matrix were 16.57 and 2.02, respectively. The overall void ratios of the sand–marine clay mixtures were 1.61, 1.20, and 0.80 for the sand fractions of 20%, 40%, and 60%, respectively (the values for sand–bentonite mixtures were 8.27, 5.79, and 4.13 for the sand fractions of 50%, 65%, and 75%). The discretized domain contained 201 nodes, with a surcharge loading of 5.0 kPa applied on the top surface, followed by the loading steps of 10, 25, 50, 100, 200, and 400 kPa.

Fig. 14 presents a comparison between the experimental data and the model simulations in the semilogarithmic compression plane v: $\ln \sigma'$ (based on Lagrangian coordinates). The compression data are associated with the reference time lines, and the simulated curves correspond to the equivalent time less than zero. The final simulated results agreed well with the experimental data. The simulated consolidation curves based on Lagrangian coordinate at different stress levels are shown in Fig. 15 in terms of the consolidation time and overall strain in the current loading step. It is seen that the effect of the sand fraction on the consolidation behavior of the sand–clay mixtures can be well reproduced by the proposed model. The experimental data and the corresponding simulation results of sand-marine clay mixtures are summarized in Figs. 16 and 17, which also shows a good consistency. The simulation consolidation curves based on Eulerian coordinates are also provided for comparison (see Fig. 18 for the simulated results and test data of the sand–bentonite mixtures).

To assess the capability of the proposed models, the simulated curves were compared against the measured strain to examine the relative errors. The relative error (RE) is defined as (Fig. 19)

$$\mathrm{RE} = \frac{\sum_{i=1}^{N} |\varepsilon_{\mathrm{model}} - \varepsilon_{\mathrm{test}}|}{\sum_{i=1}^{N} \varepsilon_{\mathrm{test}}} \tag{39}$$

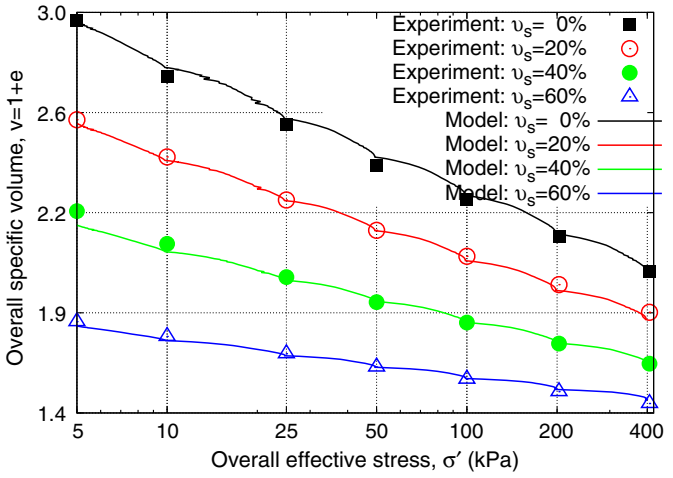

Fig. 16. Comparison between the experimental data and the model simulation in v-σ' compression plane (sand–marine clay mixtures).

J. Eng. Mech., 2019, 145(8): 04019059

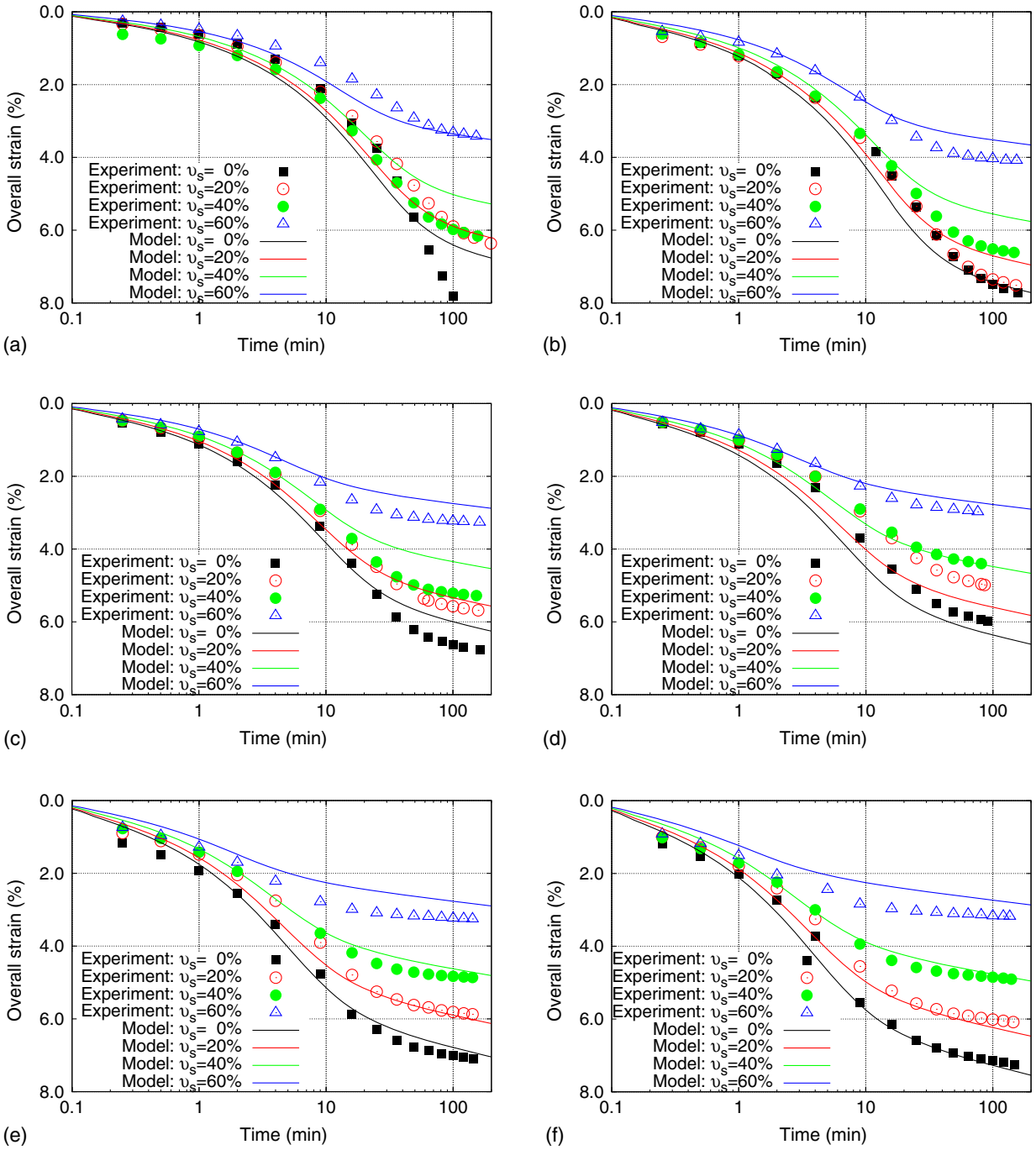

Fig. 17. Comparison between the experimental data and the model simulation based on Lagrangian coordinates (sand–marine clay mixtures): (a) 5–10 kPa; (b) 10–25 kPa; (c) 25–50 kPa; (d) 50–100 kPa; (e) 100–200 kPa; and (f) 200–400 kPa.

where ε_{model} is the overall strain of the mixture computed from the models; ε_{test} is the overall strain from interpolation of the test data; and N = number of equidistant points sampled from the consolidation curves (14 points are used in this work for calculation of the relative error). The relative errors of the proposed models are shown in Fig. 20. The relative error of the EVP model based on Lagrangian coordinates was significantly lower than that based on Eulerian coordinates, and the difference increased with the effective stress level. This is due to the decrease of the thickness of the samples, which cannot be incorporated into the model using Eulerian coordinates.

Previous EVP models have been proposed for soil with a predefined composition. For sand–clay mixtures, the model parameters based on classical EVP models have to change with the sand fraction. These models have several drawbacks: (1) to correlate the model parameters with the sand mass fractions, one must perform many oedometer tests on sand–clay mixtures with a wide range of sand fractions, which is time consuming. (2) Empirical equations used for the previous correlations are based on mass fraction of sand. However, the model parameters should depend on the volume fraction of sand, which changes during the consolidation process. (3) The empirical correlation will introduce additional parameters that do not always have concrete physical meanings. The proposed model in this study overcomes the previous shortcomings. Only two multistage oedometer tests (including unloading stages) need to be performed for calibrating the model parameters, which makes the model more suitable for field analysis by engineers.

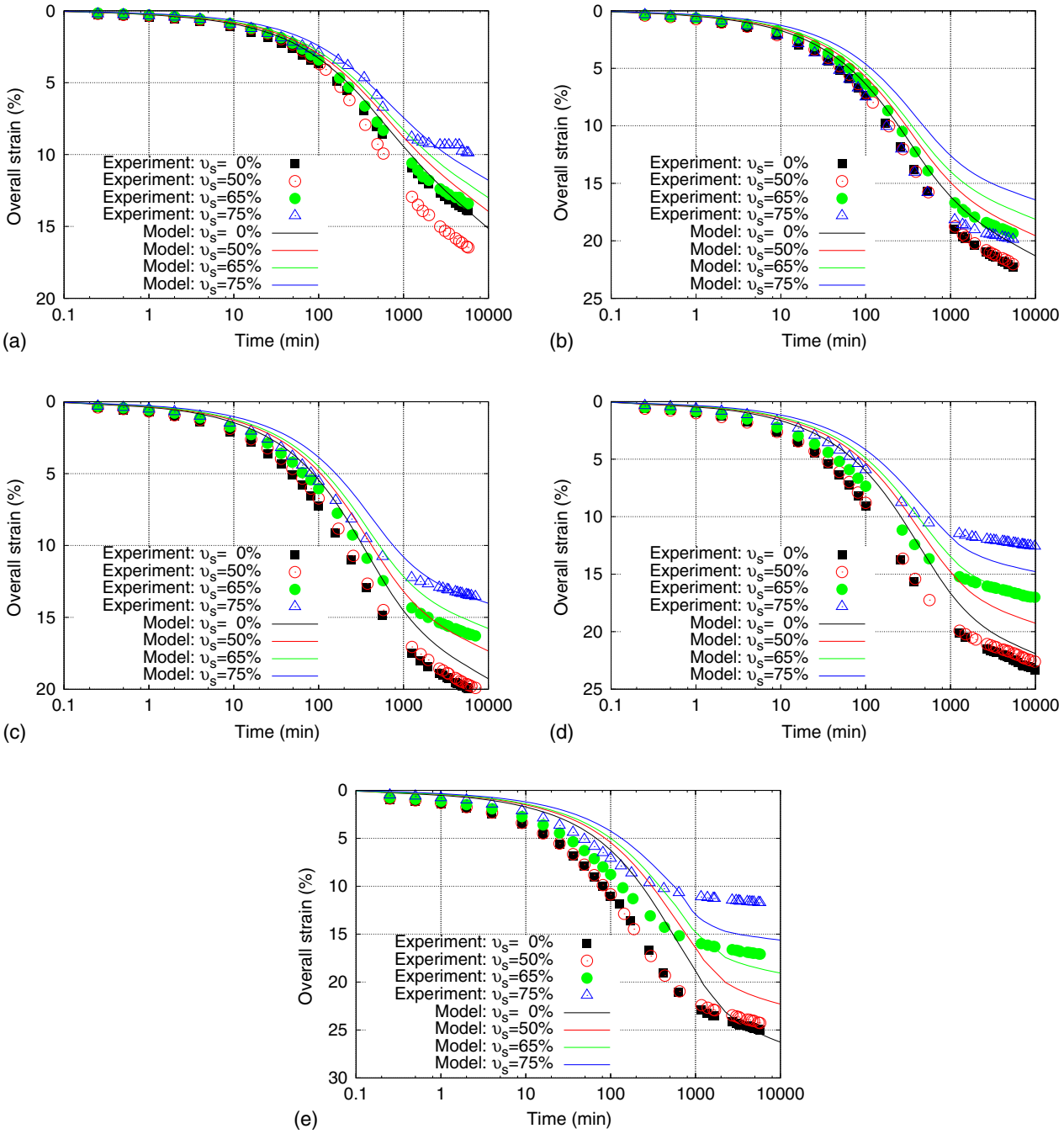

Fig. 18. Comparison between the experimental data and the model simulation based on Eulerian coordinates (sand–bentonite mixtures): (a) 5–10 kPa; (b) 10–25 kPa; (c) 25–50 kPa; (d) 50–100 kPa; and (e) 100–200 kPa.

Conclusion

A new elastic visco-plastic model considering both small and finite strains was proposed for the time-dependent stress–strain behavior of sand–clay mixtures. The EVP model was applied in a one-dimensional finite strain consolidation analysis of mixtures and was further benchmarked and validated using a finite difference method. The following conclusions are drawn:

1. Our new 1D EVP model simulation results reveal that the sand fraction significantly affects the pore water dissipation in a sand–clay mixture. This is indeed consistent with the fact that the rate of consolidation becomes faster with the increase of sand fraction, which causes a higher local void ratio and higher permeability of the mixture.
2. Benchmark analysis of the proposed model in a 1D consolidation analysis revealed that the dissipation of the excess pore water pressure using Lagrangian coordinates is more rapid than the one based on Eulerian coordinates due to the decreasing thickness of the consolidating soil layer.
3. The proposed 1D EVP model has eight parameters. The structure parameter responsible for the intergranular structure can be calibrated based on the reference time line of the mixture with a predefined sand fraction. The other parameters can be derived from the compressibility and consolidation curves of the clay matrix.

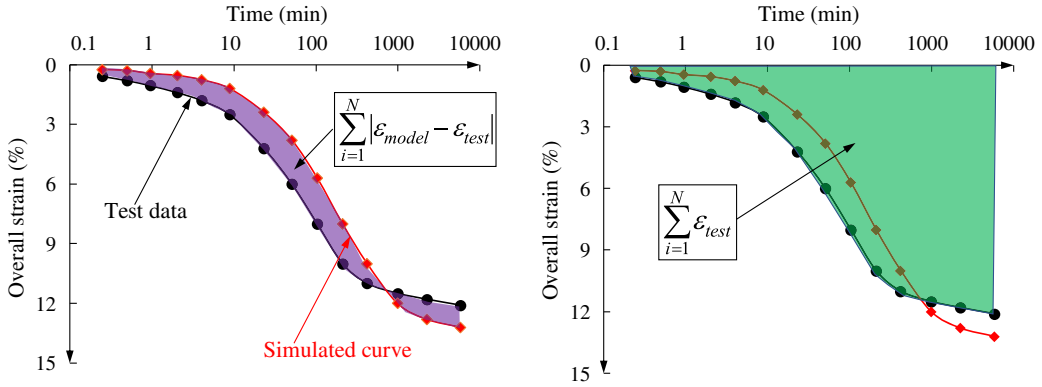

Fig. 19. Schematic figure for the calculation of the relative errors.

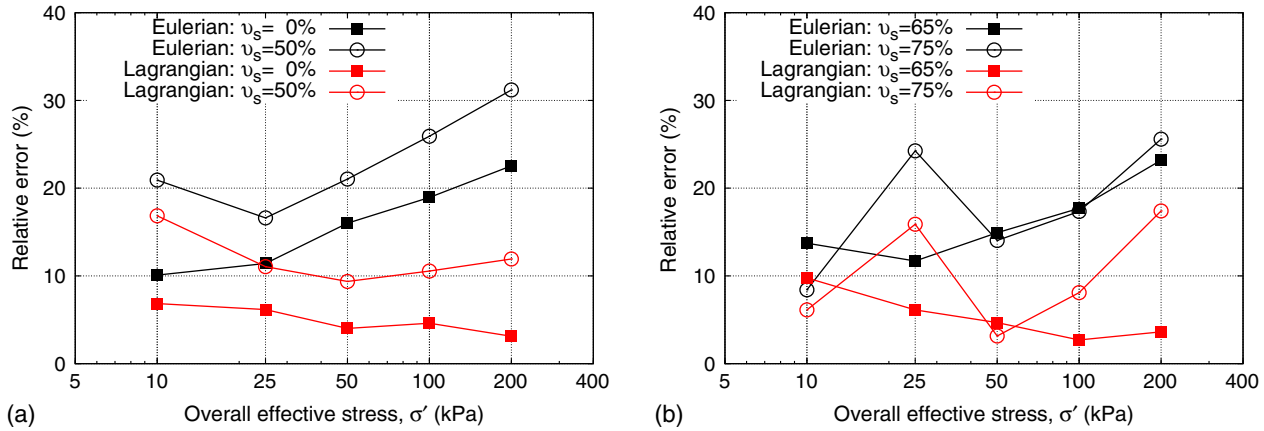

Fig. 20. Comparison of relative errors between the Lagrangian-based and Eulerian-based models: (a) $\upsilon_s = 0\%$, $\upsilon_s = 50\%$; and (b) $\upsilon_s = 65\%$, $\upsilon_s = 75\%$.

4. Experimental data of sand–bentonite mixtures and sand–marine clay mixtures have been used for validation of the proposed model. The sand fraction effects can be well reproduced by the proposed model in Lagrangian coordinates.

Appendix. Derivation of the Governing Equation [Eq. (28)]

Combining Eqs. (13), (14), (26), and (27), one obtains

$$\frac{(1+e_0)^2}{(1+e)m_v}\frac{\partial}{\partial\zeta}\left(\frac{k_c}{\gamma_w(1+e)}\frac{\partial p}{\partial\zeta}\right) = (1-\phi_s)\mu_\sigma^c\frac{\partial p}{\partial t} - (1-\phi_s)\frac{\sigma_c'\psi_c}{\kappa_c t_0}\exp\left(\frac{v_c-N_c}{\psi_c}\right)\left(\frac{\sigma_c'}{\sigma_r}\right)^{\frac{\lambda_c}{\psi_c}} \tag{40}$$

Considering the effective stress concept, it follows

$$\frac{(1+e_0)^2}{(1+e)m_v}\frac{\partial}{\partial\zeta}\left(\frac{\sigma' k_c}{\gamma_w(1+e)}\frac{\partial\ln(\sigma')}{\partial\zeta}\right) = (1-\phi_s)\sigma'\mu_\sigma^c\frac{\partial\ln(\sigma')}{\partial t} + (1-\phi_s)\frac{\sigma_c'\psi_c}{\kappa_c t_0}\exp\left(\frac{v_c-N_c}{\psi_c}\right)\left(\frac{\sigma_c'}{\sigma_r}\right)^{\frac{\lambda_c}{\psi_c}} \tag{41}$$

The value $(\sigma' k_c)/[\gamma_w(1+e)]$ is closely related to the coefficient of consolidation, which is approximately constant for a stress increment during consolidation process. Hence, Eq. (41) is rearranged as

$$\frac{(1+e_0)^2 k_c}{(1+e)^2\gamma_w m_v}\frac{\partial}{\partial\zeta}\left(\frac{\partial\ln(\sigma')}{\partial\zeta}\right) = (1-\phi_s)\mu_\sigma^c\frac{\partial\ln(\sigma')}{\partial t} + (1-\phi_s)\frac{\sigma_c'\psi_c}{\sigma' k_c t_0}\exp\left(\frac{v_c-N_c}{\psi_c}\right)\left(\frac{\sigma_c'}{\sigma_r}\right)^{\frac{\lambda_c}{\psi_c}} \tag{42}$$

Acknowledgments

The work in this paper was partially supported by the National Natural Science Foundation of China (Grant No. 51679207) and the Research Grants Council of Hong Kong (RGC/GRF Grant No. 16210017, TBRS Grant No. T22-603/15N, and CRF Grant No. C6012-15G). This work was also supported by a National State Key Project "973" grant (Grant No. 2014CB047000, subproject No. 2014CB047001) from the Ministry of Science and Technology of the People's Republic of China, a Collaborative Research Fund (CRF) project (Grant No. PolyU12/CRF/13E) and a Theme-based Research Scheme (Grant No. T22-603/15-N) from the Research Grants Council (RGC) of the Hong Kong Special Administrative Region Government (HKSARG) of China, and two GRF projects (PolyU 152196/14E; PolyU 152796/16E) from RGC of HKSARG

of China. The first author also acknowledges the financial support from the Vice-President for Research and Graduate Studies (VPRG) Office of Hong Kong University of Science and Technology (HKUST) for his Research Assistant Professor position, and the Research Institute for Sustainable Urban Development of Hong Kong Polytechnic University (Grant Nos. 1-ZVCR, 1-ZVEH, 4-BCAU, 4-BCAW, 5-ZDAF, G-YN97).

References

Anderson, M. T., and N. Lu. 2001. "Role of microscopic physicochemical forces in large volumetric strains for clay sediments." *J. Eng. Mech.* 127 (7): 710–719. https://doi.org/10.1061/(ASCE)0733-9399(2001)127:7(710).

Bian, X., Y. P. Cao, Z. F. Wang, G. Q. Ding, and G. H. Lei. 2017. "Effect of super-absorbent polymer on the undrained shear behavior of cemented dredged clay with high water content." *J. Mater. Civ. Eng.* 29 (7): 04017023. https://doi.org/10.1061/(ASCE)MT.1943-5533.0001849.

Bian, X., Y. J. Cui, and X. Z. Li. 2019. "Voids effect on the swelling behaviour of compacted bentonite." *Géotechnique* 28. https://doi.org/10.1680/jgeot.17.

Bjerrum, L. 1967. "Engineering geology of Norwegian normally-consolidated marine clays as related to settlements of buildings." *Géotechnique* 17 (2): 83–118. https://doi.org/10.1680/geot.1967.17.2.83.

Borja, R. I., and J. Choo. 2016. "Cam-clay plasticity, Part VIII: A constitutive framework for porous materials with evolving internal structure." *Comput. Methods Appl. Mech. Eng.* 309: 653–679. https://doi.org/10.1016/j.cma.2016.06.016.

Borja, R. I., and A. Koliji. 2009. "On the effective stress in unsaturated porous continua with double porosity." *J. Mech. Phys. Solids* 57 (8): 1182–1193. https://doi.org/10.1016/j.jmps.2009.04.014.

Chang, C., and M. D. Zoback. 2010. "Viscous creep in room-dried unconsolidated Gulf of Mexico shale (II): Development of a viscoplasticity model." *J. Petrol. Sci. Eng.* 72 (1-2): 50–55. https://doi.org/10.1016/j.petrol.2010.03.002.

Chang, W. J., C. W. Chang, and J. K. Zeng. 2014. "Liquefaction characteristics of gap-graded gravelly soils in K0 condition." *Soil Dyn. Earthquake Eng.* 56: 74–85. https://doi.org/10.1016/j.soildyn.2013.10.005.

Choo, J., and R. I. Borja. 2015. "Stabilized mixed finite elements for deformable porous media with double porosity." *Comput. Methods Appl. Mech. Eng.* 293: 131–154. https://doi.org/10.1016/j.cma.2015.03.023.

Cui, Y., D. Chan, and A. Nouri. 2017a. "Coupling of solid deformation and pore pressure for undrained deformation-a discrete element method approach." *Int. J. Numer. Anal. Methods Geomech.* 41 (18): 1943–1961. https://doi.org/10.1002/nag.2708.

Cui, Y., D. Chan, and A. Nouri. 2017b. "Discontinuum modeling of solid deformation pore-water diffusion coupling." *Int. J. Geomech.* 17 (8): 4017033. https://doi.org/10.1061/(ASCE)GM.1943-5622.0000903.

Cui, Y., C. E. Choi, L. H. D. Liu, and C. W. W. Ng. 2018. "Effects of particle size of monodispersed granular flows impacting a rigid barrier." *Nat. Hazard.* 91 (3): 1179–1201. https://doi.org/10.1007/s11069-018-3185-3.

Cui, Y., A. Nouri, D. Chan, and E. Rahmati. 2016. "A new approach to DEM simulation of sand production." *J. Petrol. Sci. Eng.* 147: 56–67. https://doi.org/10.1016/j.petrol.2016.05.007.

Cui, Y. F., X. J. Zhou, and C. X. Guo. 2017. "Experimental study on the moving characteristics of fine grains in wide grading unconsolidated soil under heavy rainfall." *J. Mt. Sci.* 14 (3): 417–431. https://doi.org/10.1007/s11629-016-4303-x.

De Jong, G., and A. Verruijt. 1965. "Primary and secondary consolidation of a spherical clay sample." In *Proc., 6th Int. Conf. Soil Mechanic and Foundation Engineering*, 254–258. Toronto: University of Toronto Press.

Deng, Y., Z. Wu, Y. Cui, S. Liu, and Q. Wang. 2017. "Sand fraction effect on hydro-mechanical behavior of sand–clay mixture." *Appl. Clay Sci.* 135: 355–361. https://doi.org/10.1016/j.clay.2016.10.017.

Dolinar, B. 2009. "Predicting the hydraulic conductivity of saturated clays using plasticity-value correlations." *Appl. Clay Sci.* 45 (1): 90–94. https://doi.org/10.1016/j.clay.2009.04.001.

Feng, S. J., X. Zhang, and B. Y. Cao. 2014. "Leachate recirculation in bioreactor landfills considering the effect of MSW settlement on hydraulic properties." *Environ. Earth Sci.* 72 (7): 2315–2323. https://doi.org/10.1007/s12665-014-3140-x.

Gibson, R. E., G. L. England, and M. J. L. Hussey. 1967. "The theory of one-dimensional consolidation of saturated clays: 1. Finite non-linear consolidation of thin homogeneous layers." *Géotechnique* 17 (3): 261–273. https://doi.org/10.1680/geot.1967.17.3.261.

González, C., J. Segurado, and J. LLorca. 2004. "Numerical simulation of elasto-plastic deformation of composites: Evolution of stress microfields and implications for homogenization models." *J. Mech. Phys. Solids* 52 (7): 1573–1593. https://doi.org/10.1016/S0022-5096(04)00008-0.

Graham, J., F. Saadat, M. N. Gray, D. A. Dixon, and Q. Y. Zhang. 1989. "Strength and volume change behaviour of a sand-bentonite mixture." *Can. Geotech. J.* 26 (2): 292–305. https://doi.org/10.1139/t89-038.

Hashin, Z. 1983. "Analysis of composite materials—A survey." *J. Appl. Mech.* 50 (3): 481–505. https://doi.org/10.1115/1.3167081.

Hawlader, B. C., B. Muhunthan, and G. Imai. 2003. "Viscosity effects on one-dimensional consolidation of clay." *Int. J. Geomech.* 3 (1): 99–110. https://doi.org/10.1061/(ASCE)1532-3641(2003)3:1(99).

He, B., B. Mortazavi, X. Zhuang, and T. Rabczuk. 2016. "Modeling Kapitza resistance of two-phase composite material." *Compos. Struct.* 152: 939–946. https://doi.org/10.1016/j.compstruct.2016.06.025.

Hinchberger, S. D., G. Qu, and K. Y. Lo. 2010. "Constitutive approach for rate-sensitive anisotropic structured clays." *Int. J. Numer. Anal. Methods Geomech.* 34 (17): 1797–1830. https://doi.org/10.1002/nag.881.

Hong, Z., J. Yin, and Y. J. Cui. 2010. "Compression behavior of reconstituted soils at high initial water contents." *Géotechnique* 60 (9): 691–700. https://doi.org/10.1680/geot.09.P.059.

Horpibulsuk, S., M. D. Liu, Z. Zhuang, and Z. S. Hong. 2016. "Complete compression curves of reconstituted clays." *Int. J. Geomech.* 16 (6): 06016005. https://doi.org/10.1061/(ASCE)GM.1943-5622.0000663.

Huang, J., X. Xie, J. Zhang, J. Li, and W. Wang. 2014. "Nonlinear finite strain consolidation analysis with secondary consolidation behavior." *Math. Prob. Eng.* 2014: 1–8. https://doi.org/10.1155/2014/979380.

Hubert, J., X. F. Liu, and F. Collin. 2016. "Numerical modeling of the long-term behavior of municipal solid waste in a bioreactor landfill." *Comput. Geotech.* 72: 152–170. https://doi.org/10.1016/j.compgeo.2015.10.007.

Imai, G., Y. Tanaka, and H. Saegusa. 2003. "One-dimensional consolidation modeling based on the isotach law for normally consolidated clays." *Soils Found.* 43 (4): 173–188. https://doi.org/10.3208/sandf.43.4_173.

Kumar, G. V. 1996. "*Some aspects of the mechanical behavior of mixtures of kaolin and coarse sand*." Ph.D. dissertation, Dept. Infrastructure and Environment, Univ. of Glasgow.

Marques, A. C. M., G. M. Filz, and O. M. Vilar. 2003. "Composite compressibility model for municipal solid waste." *J. Geotech. Geoenviron. Eng.* 129 (4): 372–378. https://doi.org/10.1061/(ASCE)1090-0241(2003)129:4(372).

Mesri, G. 2003. "Primary compression and secondary compression." In *Soil behavior and Soft Ground Construction*, 122–166. Reston, VA: ASCE.

Mesri, G., and A. Castro. 1987. "Cα/Cc concept and K0 during secondary compression." *J. Geotech. Eng.* 113 (3): 230–247. https://doi.org/10.1061/(ASCE)0733-9410(1987)113:3(230).

Mesri, G., and P. M. Godlewski. 1977. "Time and stress-compressibility interrelationship." *J. Geotech. Geoenviron. Eng. Div.* 103 (5): 417–430.

Mesri, G., and R. E. Olson. 1971. "Mechanisms controlling the permeability of clays." *Clays Clay Miner.* 19 (3): 151–158. https://doi.org/10.1346/CCMN.1971.0190303.

Mitchell, J. K. 1993. *Fundamentals of soil behavior*. New York: Wiley.

Monkul, M. M., and G. Ozden. 2005. "Effect of intergranular void ratio on one-dimensional compression behavior." In Vol. 3 of *Proc., Int. Conf. on Problematic Soils*, 1203–1209. Famagusta: International Society of Soil Mechanics and Geotechnical Engineering, Turkish Republic of Northern Cyprus.

Monkul, M. M., and G. Ozden. 2007. "Compressional behavior of clayey sand and transition fines content." *Eng. Geol.* 89 (3): 195–205. https://doi.org/10.1016/j.enggeo.2006.10.001.
Ng, T. T., W. Zhou, and X. L. Chang. 2016. "Effect of particle shape and fine content on the behavior of binary mixture." *J. Eng. Mech.* 143 (1): C4016008. https://doi.org/10.1061/(ASCE)EM.1943-7889.0001070.
Pane, V., and R. L. Schiffman. 1997. "The permeability of clay suspensions." *Géotechnique* 47 (2): 273–288. https://doi.org/10.1680/geot.1997.47.2.273.
Puppala, A. J., A. Pedarla, A. Pino, and L. R. Hoyos. 2017. "Diffused double-layer swell prediction model to better characterize natural expansive clays." *J. Eng. Mech.* 143 (9): 04017069. https://doi.org/10.1061/(ASCE)EM.1943-7889.0001292.
Quayum, M. S., X. Zhuang, and T. Rabczuk. 2015. "Computational model generation and RVE design of self-healing concrete." *Front. Struct. Civ. Eng.* 9 (4): 383–396. https://doi.org/10.1007/s11709-015-0320-z.
Satyanaga, A., H. Rahardjo, E. C. Leong, and J. Y. Wang. 2013. "Water characteristic curve of soil with bimodal grain-size distribution." *Comput. Geotech.* 48: 51–61. https://doi.org/10.1016/j.compgeo.2012.09.008.
Shi, X. S., and I. Herle. 2015. "Compression and undrained shear strength of remoulded clay mixtures." *Géotech. Lett.* 5 (2): 62–67. https://doi.org/10.1680/geolett.14.00089.
Shi, X. S., and I. Herle. 2017. "Numerical simulation of lumpy soils using a hypoplastic model." *Acta Geotech.* 12 (2): 349–363. https://doi.org/10.1007/s11440-016-0447-7.
Shi, X. S., I. Herle, and D. Muir Wood. 2018a. "A consolidation model for lumpy composite soils in open-pit mining." *Géotechnique* 68 (3): 189–204. https://doi.org/10.1680/jgeot.16.P.054.
Shi, X. S., and J. Yin. 2017. "Experimental and theoretical investigation on the compression behavior of sand-marine clay mixtures within homogenization framework." *Comput. Geotech.* 90: 14–26. https://doi.org/10.1016/j.compgeo.2017.05.015.
Shi, X. S., and J. Yin. 2018c. "Consolidation behavior for saturated sand-marine clay mixtures considering the intergranular structure evolution." *J. Eng. Mech.* 144 (2): 04017166. https://doi.org/10.1061/(ASCE)EM.1943-7889.0001391.
Shi, X. S., and J. Yin. 2018b. "Estimation of hydraulic conductivity of saturated sand–marine clay mixtures with a homogenization approach." *Int. J. Geomech.* 18 (7): 04018082. https://doi.org/10.1061/(ASCE)GM.1943-5622.0001190.
Shi, X. S., J. H. Yin, W. Q. Feng, and W. B. Chen. 2018d. "Analysis of the creep coefficient of binary sand-bentonite mixtures in oedometer condition using mixture theory." *Int. J. Geomech.* 18 (12): 04018159. https://doi.org/10.1061/(ASCE)GM.1943-5622.0001295.
Silva, S. D. 2016. *Three runway system project (3RS project), contract 3206-main reclamation works*. Rep. for ZHECC-CCCC-CDC joint venture. 7076481/R00. Hong Kong.
Singh, R. P., M. Singh, and C. P. Ojha. 2014. "An experimental study on consolidation of compacted clays." *Int. J. Geotech. Eng.* 8 (1): 112–117. https://doi.org/10.1179/1938636213Z.00000000052.
Tandon, G. P., and G. J. Weng. 1988. "A theory of particle-reinforced plasticity." *ASME J. Appl. Mech.* 55 (1): 126–135.
Tu, S. T., W. Z. Cai, Y. Yin, and X. Ling. 2005. "Numerical simulation of saturation behavior of physical properties in composites with randomly distributed second-phase." *J. Compos. Mater.* 39 (7): 617–631. https://doi.org/10.1177/0021998305047263.
Valliappan, S., and N. Khalili-Naghadeh. 1990. "Flow through fissured porous media with deformable matrix." *Int. J. Numer. Methods Eng.* 29 (5): 1079–1094. https://doi.org/10.1002/nme.1620290512.
Xie, K. H., and C. J. Leo. 2004. "Analytical solutions of one-dimensional large strain consolidation of saturated and homogeneous clays." *Comput. Geotech.* 31 (4): 301–314. https://doi.org/10.1016/j.compgeo.2004.02.006.
Yin, J. H. 1999a. "Non-linear creep of soils in oedometer tests." *Géotechnique* 49 (5): 699–707. https://doi.org/10.1680/geot.1999.49.5.699.
Yin, J. H. 1999b. "Properties and behavior of Hong Kong marine deposits with different clay contents." *Can. Geotech. J.* 36 (6): 1085–1095. https://doi.org/10.1139/t99-068.
Yin, J. H., and W. Q. Feng. 2017. "A new simplified method and its verification for calculation of consolidation settlement of a clayey soil with creep." *Can. Geotech. J.* 54 (3): 333–347. https://doi.org/10.1139/cgj-2015-0290.
Yin, J. H., and J. Graham. 1994. "Equivalent times and one-dimensional elastic viscoplastic modelling of time-dependent stress–strain behaviour of clays." *Can. Geotech. J.* 31 (1): 42–52. https://doi.org/10.1139/t94-005.
Yin, J. H., and J. Graham. 1996. "Elastic visco-plastic modelling of one-dimensional consolidation." *Géotechnique* 46 (3): 515–527. https://doi.org/10.1680/geot.1996.46.3.515.
Zeng, L. L., Z. S. Hong, and F. Q. Chen. 2012. "A law of change in permeability coefficient during compression of remolded clays." *Rock Soil Mech.* 33 (5): 1286–1292.
Zeng, L. L., Z. S. Hong, and Y. J. Cui. 2016. "Time-dependent compression behaviour of dredged clays at high water contents in China." *Appl. Clay Sci.* 123: 320–328. https://doi.org/10.1016/j.clay.2016.01.039.
Zhao, M., Q. Zhang, S. Li, and H. Zhao. 2017. "Investigation on coupled fluid-flow and stress in dual model rock mass with time-dependent effect and its simulation." *Geosciences* 7 (3): 45. https://doi.org/10.3390/geosciences7030045.
Zhou, Z., H. Yang, X. Wang, and B. Liu. 2016. "Model development and experimental verification for permeability coefficient of soil-rock mixture." *Int. J. Geomech.* 17 (4): 04016106. https://doi.org/10.1061/(ASCE)GM.1943-5622.0000768.
Zhuang, X., R. Huang, C. Liang, and T. Rabczuk. 2014. "A coupled thermo-hydro-mechanical model of jointed hard rock for compressed air energy storage." *Math. Prob. Eng.* 2014: 1–11.
Zhuang, X., Q. Wang, and H. Zhu. 2015. "A 3D computational homogenization model for porous material and parameters identification." *Comput. Mater. Sci.* 96: 536–548. https://doi.org/10.1016/j.commatsci.2014.04.059.
Zhuang, X., Q. Wang, and H. Zhu. 2017. "Effective properties of composites with periodic random packing of ellipsoids." *Materials* 10 (2): 112. https://doi.org/10.3390/ma10020112.